Materials Advances

ROYAL SOCIETY OF CHEMISTRY

PAPER

View Article Online
View Journal | View Issue

Cite this: *Mater. Adv.*, 2025, 6, 224

Synthesis of a $BiSbS_3$@$BiSbO_4$/CNH nanocomposite for wastewater treatment and electrochemical application†

Maria Batool [a] and Muhammad Nadeem Zafar *[ab]

Due to the toxic effects of pentachlorophenol (5-CP), its degradation *via* photocatalysis is significant because photocatalysis is ecofriendly and cost effective. However, the majority of photocatalysts have a tendency for recombination of fast charge carriers, which limit their efficacy. To combat this issue, a carbon nanohorn (CNH)-modified $BiSbS_3$/$BiSbO_4$ ($BiSbS_3$@$BiSbO_4$/CNH) nanocomposite was synthesized by hydrothermal method to degrade the endocrine disrupting agent 5-CP. Structural composition, morphology, porosity as well as optical characteristics of the $BiSbS_3$@$BiSbO_4$/CNH nanocomposite (B@B/CNH) were analyzed *via* different characterization techniques. B@B/CNH was observed to have a low band gap of 2.64 eV compared to its counterparts $BiSbS_3$ (BSbS), $BiSbO_4$ (BSbO), and BSbO/CNH, which indicated its efficient photocatalytic potential. Various reaction factors like pH, B@B/CNH dosage, 5-CP concentration, and time were optimized, and B@B/CNH exhibited 93% efficiency at pH 6 and a dosage of 0.1 g L^{-1} for the degradation of 10 ppm 5-CP under visible light irradiation for 140 minutes, exceeding that of their counterparts BSbO/CNH (84%), BSbS (82%) and BSbO (81%). The kinetic study showed that the degradation of 5-CP followed the pseudo-first-order model with R^2 = 0.975. A scavenger study was performed to gain insights into the mechanistic path, which indicated that all the charge carriers, like holes, electrons, oxide radicals and hydroxyl radicals, are involved in the photodegradation, but among them, oxide radicals played the most prominent role during the photocatalysis process. Further, the effect of other phenolic pollutants on the degradation of 5-CP was evaluated, which indicated that B@B/CNH can be employed for the eradication of other pollutants along with 5-CP. Additionally, the degradation behavior of 5-CP was evaluated by density functional theory (DFT), which was in line with the results obtained from the scavenger study. Additionally, an electrochemical study was performed for B@B/CNH to understand its electrochemical performance for supercapacitor applications.

Received 9th October 2024,
Accepted 12th November 2024

DOI: 10.1039/d4ma01017e

rsc.li/materials-advances

1. Introduction

Endocrine disrupting agents (EDAs) are substances which tamper with the endocrine system and control hormone levels in both humans and animals as it gets accumulated into the human body irreversibly. These chemicals could mimic hormones, inhibit hormone receptors and cause hormone-induced cancers. EDAs have been found to be associated with a decrease in the quality of sperm and increase in secretion disorders.[1,2] Fast industrialization has been one of the reasons for the addition of EDAs into water bodies. Waste water discharge may contain radioactive materials, organic pollutants, phenolic compounds, and heavy metals.[3–6] The degradation of phenolic compounds, for example, pentachlorophenol (5-CP),[7] pyrocatechol,[8] 2,4-di-chlorophenol,[9] 4-chlorophenol[10] and bisphenol A,[11] is of prime importance due to their high toxicity and prolonged exposure. Among these, 5-CP can cause endocrine disruption and is considered the most toxic due to its extremely resistant nature and long half-life. Furthermore, the heavy use of 5-CP makes this problem worse, which can be related to its production of about 18136890.91 kg per year as pesticide in the United States. 5-CP can also make its way into water bodies *via* wood industry and as a fungicide.[12,13]

The route of exposure dictates the ability of 5-CP to affect human beings (Fig. 1),[14] and when exposed to 5-CP at work, workers may develop peripheral neuropathy, chronic liver damage, leukemia and embryotoxicity.[14] The presence of 5-CP in the environment and people was thought to be connected with the schistosomiasis outbreak. In China's schistosomiasis-

[a] *Department of Chemistry, University of Gujrat, Gujrat 50700, Pakistan. E-mail: znadeempk@gmail.com, nadeem.zafar@uog.edu.pk*
[b] *State Key Laboratory of Electroanalytical Chemistry, Changchun Institute of Applied Chemistry, Chinese Academy of Sciences, 5625 Renmin Street, Changchun 130022, People's Republic of China*

† Electronic supplementary information (ESI) available: Section S1–S4, Fig. S1–S9 and Tables S1–S3. See DOI: https://doi.org/10.1039/d4ma01017e

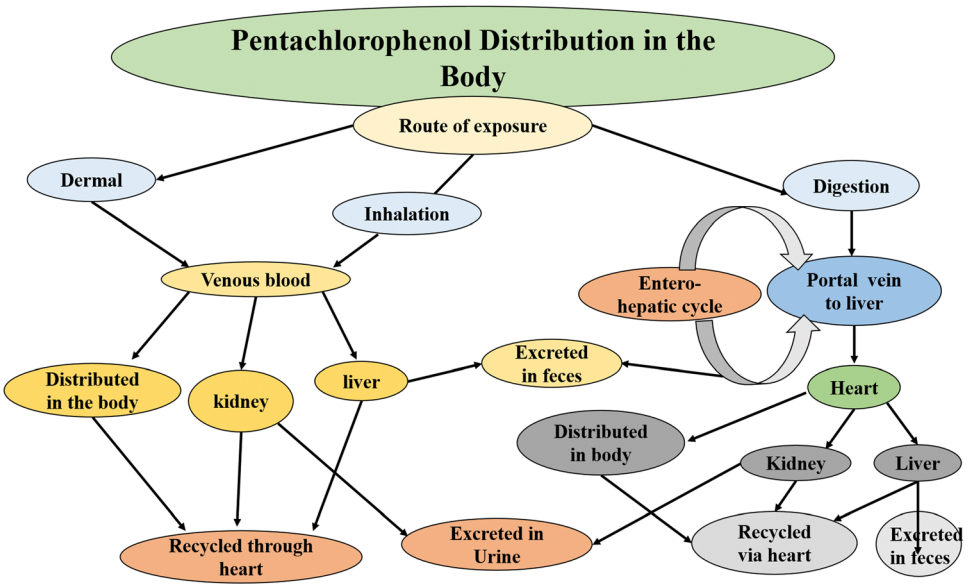

Fig. 1 Distribution of pentachlorophenol based on exposure route. Reproduced from Reference[14] with permission from Elsevier B.V. Copyright [1991].

epidemic areas, it has been noted that 5-CP, even at low ambient levels, can cause cancer and thyroid disruption.[15] As a result, the removal of 5-CP from aqueous solutions has become a vital issue and due to its extreme toxicity and persistent nature, reliable techniques are needed for its eradication without causing secondary contamination. Several techniques such as bioremediation,[16] oxidation,[17] adsorption,[18] and electrochemical approaches[19] have been tested to remove 5-CP and other pollutants from wastewater. Among them, biodegradation has been widely reported to eradicate 5-CP[20–24] and adsorption/photocatalysis have been determined to be the most reliable methods due to their good efficiency, simplicity, and cost effectiveness.[25–27] However, adsorption does not involve degradation into safer products, only the transportation of 5-CP from one source to another. This makes photocatalysis the most suitable process due to its capability to degrade pollutants with proven efficacy.

To date, different studies on metal-based heterojunction nanocomposites for the photodegradation of 5-CP are available in the literature. In this context, the synthesis of Bi/SnO_2/TiO_2 graphene was reported, which showed 84% degradation of 5-CP under visible light.[28] Similarly, the synthesis of Bi_2O_3/TiO_2–montmorillonite nanocomposites was reported for the degradation of 5-CP. TiO_2-montmorillonite showed 78% degradation of 5-CP and Bi_2O_3/TiO_2–montmorillonite nanocomposites showed a degradation of 84% 5-CP. This indicates that the inclusion of Bi_2O_3 can increase the efficacy of photocatalysts.[29] The ternary heterojunction of $FeNi_3$/SiO_2/ZnO was reported to show 100% degradation for 5-CP in 180 min.[30] In the same perspective, commercial TiO_2 was prepared *via* the hydrothermal method, followed by the deposition of silver, which exhibited around 99% of degradation of 5-CP in 180 min.[31] However, these reported works have room for improvement in terms of cost effectiveness, amount of photocatalyst, irradiation time and degradation efficacy, making it necessary to synthesize photocatalysts that can overcome most of the shortcomings of traditional photocatalysts.

According to our thorough inquiries, carbon nanohorns (CNH), $BiSbS_3$ (BSbS), $BiSbO_4$ (BSbO), and $BiSbS_3$@$BiSbO_4$/CNH nanocomposite (B@B/CNH) have never been investigated for the photodegradation of 5-CP. Thus, herein, CNH and CNH-based nanomaterials/nanocomposites were investigated for the degradation of 5-CP and various other contaminants due to their excellent characteristics such as good mechanical strength, stability, and durability. The current work will ensure the addition of novel photocatalysts through reliable synthetic schemes. Additionally, the electrochemical studies of B@B/CNH will inspire researchers to employ CNH-based nanocomposites for applications related to supercapacitors. In the present work, BSbO, BSbS, BSbO/CNH and B@B/CNH were synthesized and employed for the photodegradation of 5-CP under visible light. The B@B/CNH photocatalyst showed the ability to inhibit the fast recombination of charge carriers and increase the adsorption of visible light due to its large surface area induced by the inclusion of CNH. To imitate actual wastewater conditions, the degradation of 5-CP by B@B/CNH was executed in the presence of other pollutants (phenolic compounds). Moreover, a theoretical study *via* density functional theory (DFT) was performed to predict the photo-degradation behavior of 5-CP by B@B/CNH. In addition, electrochemical studies were executed to assess the electronic properties of B@B/CNH in relation to supercapacitors.

2. Materials and methods

2.1 Chemicals

All chemicals employed in this project were of analytical grade and used without additional purification. The detail information about the chemicals can be found in Section S1 (ESI†).

2.2 Synthesis of $BiSbS_3$@$BiSbO_4$/CNH nanocomposite (B@B/CNH)

The procedure for the synthesis of B@B/CNH involved a four-step processes, which involved the hydrothermal method and stirring technique, making it very simple and economic due to the absence of difficult strategies during the scheme.

2.2.1 Production of $BiSbO_4$ (BSbO). The synthesis of BSbO was performed *via* the hydrothermal strategy (Scheme 1-I). Firstly, 0.5 M solutions of both $SbCl_3$ and $BiCl_3$ were mixed, followed by the addition of HCl for homogeneity and the resulting mixture was stirred for 60 min to increase its homogeneity. The basic pH of the mixture was attained *via* the dropwise addition of NaOH solution, while stirring for 40 min. Then, the resulting mixture was stirred vigorously and moved to an autoclave for 360 min at 180 °C. Finally, the product was centrifuged, washed and dried in an oven at 60 °C. The obtained product (BSbO) was calcined for 300 min at 600 °C to eradicate any formed hydroxides.

2.2.2 Production of $BiSbS_3$ (BSbS). In the 2nd step, BSbS was prepared *via* the hydrothermal method (Scheme 1-II). In the synthesis of BSbS, an aqueous solution of $Bi(NO_3)_3{\cdot}5H_2O$ was formed by adding 0.7 g of salt with 0.1 M HCl into 30 mL water. Similarly, 30 mL aqueous solution of $SbCl_3$ was prepared by dissolving 1.3 g of salt. Both solutions were stirred for 30 min, followed by the addition of bismuth nitrate solution into the antimony chloride solution. Then, 15 mL of 0.8 M thioacetamide was added to the resulting mixture, and after the mixture was stirred for 60 min. After stirring, the solution was placed in an autoclave for 12 h at 180 °C. The synthesized product (BSbS) was centrifuged, washed and dried at 60 °C.

2.2.3 Modification of BSbO by carbon nanohorns (CNH). In the 3rd phase, BSbO was modified by CNH using a hydrothermal system (Scheme 2-I). For the synthesis of BSbO/CNH, a suspension of CNH (10 g L^{-1}) was sonicated for 40 min followed by the addition of 10 mL of glutaraldehyde (linker agent). Then, 0.2 g of prepared BSbO was poured into a solution of CNH followed by stirring for 60 min. The resulting mixture was transferred to an autoclave for 240 min at 180 °C. The obtained CNH-modified product BSbO/CNH was centrifuged, washed and dried at 60 °C.

2.2.4 Synthesis of B@B/CNH. In the final phase, stirring was the main step to form the heterojunction product B@B/CNH (Scheme 2-II). This step involved the addition of 0.2 g of BSbO/CNH and 0.2 g of BSbS into ethanol separately followed by stirring for 240 min. After that, mixing of both solutions was performed, followed by stirring for 12 h. The obtained product was centrifuged, washed and dried at 60 °C. All these steps were very simple and reliable, which only involved stirring and heating in an autoclave without any complex chemicals and solvents.

2.3 Characterization

B@B/CNH was characterized using various techniques such as XRD, SEM, EDX, TEM, UV-vis, PL, FTIR, and BET. In-depth information about the instruments can be found in Section S2 (ESI†).

2.4 Photocatalytic study

In batch mode experiments, the photocatalytic activity of B@B/CNH was assessed for the degradation of 5-CP under visible light irradiation. A stock solution of 5-CP having a concentration of 1000 ppm was prepared and other solutions were prepared from the stock solution using dilution method. All experiments were carried out at room temperature. To get the ideal results, different parameters such as pH, photocatalyst dose, 5-CP concentration, and light irradiation time were optimized. Optimization of the parameters was completed by varying the pH between 2 and 10, the photocatalyst dosage between 0.02 g L^{-1} and 0.4 g L^{-1}, 5-CP concentration between 5 to 25 ppm, and irradiation time from 20 to 140 min. For these experiments (except photocatalyst dosage), suspensions of photocatalysts were prepared by dissolving 0.001 g of photocatalyst into 10 mL water, followed by stirring. For the dosage experiment, suspensions were prepared in the range of 0.02 to 0.4 g L^{-1}. In the second step, the prepared suspension was mixed in 40 mL of 10 ppm 5-CP solution and the 5-CP solution containing the photocatalyst was placed on an orbital shaker

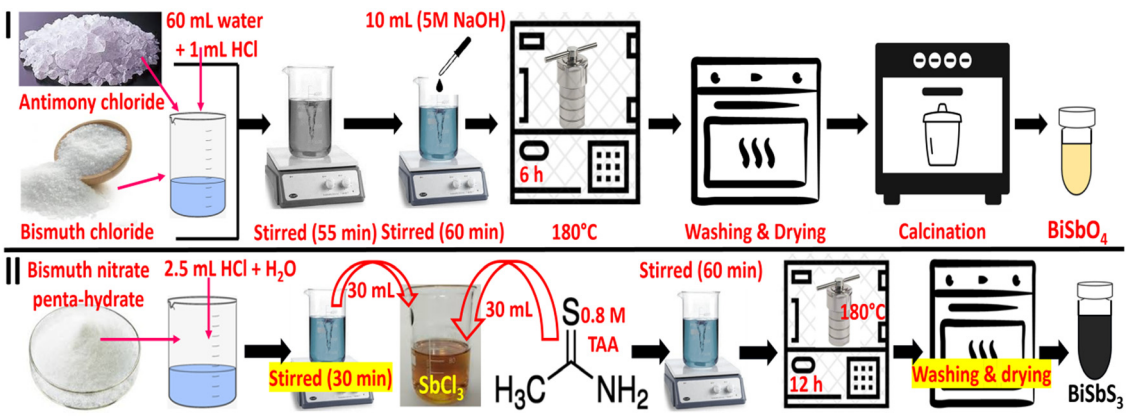

Scheme 1 Procedure for the synthesis of BSbO and BSbS nanocomposites.

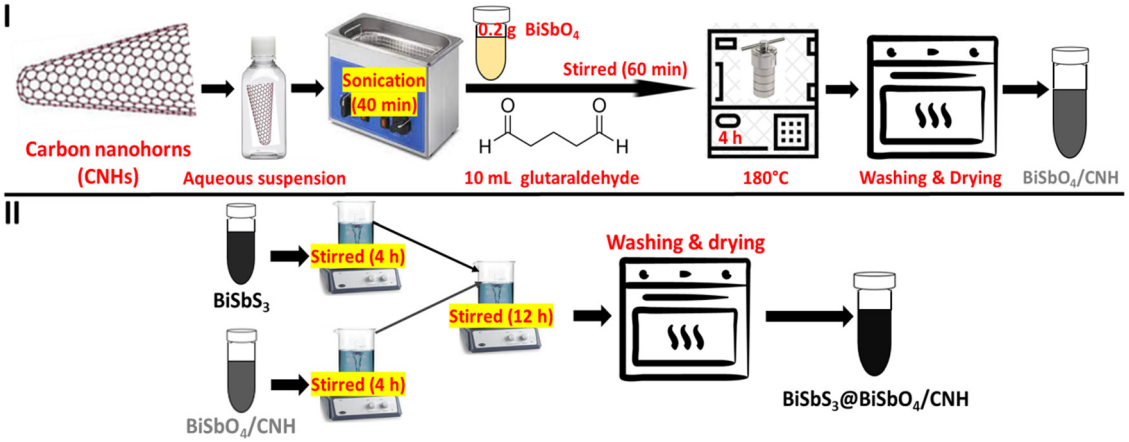

Scheme 2 Procedure for the synthesis of BSbO/CNH and B@B/CNH nanocomposites.

and left for 40 min in the dark to attain adsorptive equilibrium and any possible adsorption. After this, the reaction mixture was exposed to visible light and examined at 300 nm after every 20 min using a spectrofluorophotometer (RF-6000, Shimadzu, Columbia, USA). By employing the same catalyst three times successively, B@B/CNH was examined for its stability and recyclability to degrade 5-CP under the optimized conditions.

2.5 Recycling of B@B/CNH and scavengers/other pollutants effect on 5-CP degradation

According to the optimized experiments, it was found that B@B/CNH has superior activity towards the degradation of 5-CP. Next, the recycling capability and stability of B@B/CNH were examined, and the effect of scavengers and other pollutants on the degradation of 5-CP was also evaluated. The above-mentioned method in Section 2.4 was utilized for recycling as well the scavenger/other pollutant experiments. The B@B/CNH catalyst was collected centrifuged with water and ethanol after the photocatalyst experiment to remove the pollutant, followed by drying at 60 °C for reuse several times. The same procedure was repeated three times. The scavenger study was performed under the optimized conditions by adding 0.1 g L^{-1} of B@B/CNH suspension to 30 mL of 10 ppm 5-CP solution. Then, the resulting mixture was poured into 10 mL of 10 ppm scavenger solution. The effect of other pollutants on the degradation of 5-CP was performed by mixing 10 mL of 10 ppm other pollutants with 30 mL of 10 ppm 5-CP solution at room temperature.

2.6 Preparation of working electrode and electrochemical study

Initially, a mixture containing a minute amount of alcohol and 80 wt% (0.03 g) of B@B/CNH, 5 wt% (0.002 g) of polytetrafluoroethylene (binder) and 15 wt% (0.006 g) of carbon black (conducting agent) was prepared to construct the working electrode. The second step involved evenly spreading the produced mixture onto a 1 cm × 1 cm piece of nickel foam, and then it was dried overnight at 85 °C.[32] Moreover, the active mass applied to prepare all the working electrodes was 0.03 g cm^{-2}. In the three-electrode system, a silver–silver chloride (sat KCl) electrode was used as the reference electrode, platinum as the counter electrode and nickel foam as the working electrode to perform the electrochemical measurements (Gamry galvanostat/potentiostat interface (5000E)).

3. Result and discussion

3.1 Characterization

XRD analysis was performed to check the crystal quality and possible composition of the photocatalyst. The XRD pattern of B@B/CNH exhibited its good crystal quality due to the presence of sharp and intense peaks (Fig. 2). It was observed that the diffraction peaks of BSbO according to JCPDS card # 96-202-0156 coincided with the diffraction peaks of BSbS with different Miller indices at 2θ values of 15.70°, 25°, 26.50°, 33.50°, 34.35°, 37°, 39.5°, 40.44°, 43.65°, 46.82°, 48.75°, 50.61°, 53°, 54.20°, 56.4°, 60°, 60.60°, 62.50°, 64.44°, 66.1°, 66.75°, and 70.72°. This pattern confirmed the successful production of a heterojunction (BSbO/BSbS) in B@B/CNH. The presence of CNH was confirmed by the diffraction peak at 26° with a Miller index of (002) according to the literature.[33] The matching diffraction peak of CNH with the diffraction peak of BSbS and BSbO at

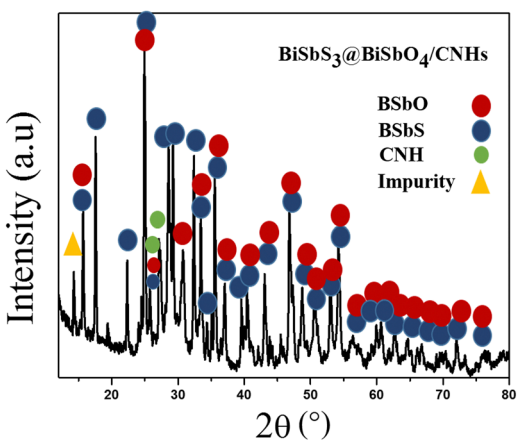

Fig. 2 XRD pattern of B@B/CNH nanocomposite.

26.3° confirmed the formation of the B@B/CNH heterojunction with the Miller index of (111). The peak at 27.30° is assigned to oxidized CNH and that at 14.30° to impurities (Fig. S1c, ESI†). The peaks in relation to BSbS are shown in Fig. 2 and a detailed depiction with the related Miller indices is presented in Fig. S1a (ESI†), according to JCPDS card no: 96-900-3467. Its phase structure was found to be orthorhombic with a density of 5.24 g cm^{-3}. According to the data sheet, there are two types of bismuth atoms, two types of antimony atoms and three types of sulphur atoms (Fig. S2a, ESI†). Type 1, type 3 and type 4 sulphur atoms and their bonding to bismuth are shown in Fig. S2b and d (ESI†). The coordination number of antimony in relation to bismuth is two (Fig. S2e, ESI†). The type 1 sulphur atom is coordinated between two antimony atoms (Fig. S2f, ESI†). The coordination number of antimony in relation to the type 2 sulphur atom is three (Fig. S2g, ESI†). The coordination number of antimony in relation the type 3 sulphur atom is two (Fig. S2h, ESI†).

The peaks obtained for BSbO are shown in Fig. 2 and the related Miller indices at the 2θ values are shown in Fig. S1b (ESI†), according to JCPDS card no: 96-591-0185. The data analysis exhibited that BSbO has a monoclinic phase and density of 16.25100 g cm^{-3}. The Vesta software was used to predict the position of the atoms and corresponding bonding in BSbO. One unit of BSbO has 15 bismuth atoms, among which eight reside at corners, one atom is body centered, two are face centered and four atoms reside at the edges (Fig. S3a, ESI†), and the antimony atoms are overlaying at the same positions as the bismuth atoms (Fig. S3d, ESI†). The other atoms were observed to be oxygen atoms, which are of five types, among which only type 1 and type 5 are visible inside the unit cell, and other oxygen atoms are out of plane. Sixteen type 1 oxygen atoms were observed to be shared between two antimony atoms, and thus the coordination number of the antimony atom for type 1 oxygen atoms will be eight (Fig. S3b, ESI†) and four type 5 oxygen atoms were seen to be coordinated to the antimony atom (Fig. S3c, ESI†). Eight type 1 oxygen atoms were seen to be shared between two bismuth atoms with a coordination number of four for each bismuth atom (Fig. S3e, ESI†) and the coordination number of bismuth with type 5 oxygen atoms is four (Fig. S3f, ESI†). The coordination number of type 1 oxygen with type 5 oxygen atoms is six (Fig. S3g and h, ESI†).

B@B/CNH was found to have a heterostructure assembly when analyzed *via* SEM to evaluate its surface structure. Three different forms of morphologies can be seen in Fig. 3, which refers to the presence of three types of composites in one nanocomposite (heterojunction) (Fig. 3(d)). As confirmed in the literature, the rod-like morphology belongs to CNH[34] (Fig. 3). As seen in Fig. 3(e), EDX analysis was performed to examine the elements and their percentages in B@B/CNH. Significant proportions of bismuth, antimony, and sulfur were present in B@B/CNH, as confirmed by the strong peaks of these elements in the EDX spectrum. Carbon has a peak that is similarly sharp, but it is smaller than that of the other elements. Fig. 3(e) displays the weight fraction of each element in B@B/CNH predicted by elemental analysis.

TEM analysis was completed to gain further insight into the morphology of B@B/CNH, as presented in Fig. 4. The morphology obtained from the TEM analysis was further confirmed by the results of the SEM analysis. TEM examination also showed the occurrence of three different types of structures, irregularly arranged flakes, rod-like structure and round deposits. The possible deposition of spherical particles onto CNH and flakes were clearly visible in Fig. 4(b) and (c), respectively. The SAED TEM image was used to calculate the inter planer distance and corresponding Miller indices from JCPDS #96-900-3467 (BSbS) and JCPDS #96-202-0156 (BSbO) (Fig. 4(e) and Table S1, ESI†). This indexing confirmed the presence of a heterojunction but with the strong presence of BSbS compared to BSbO and CNH because according to Table S1 (ESI†), the majority of indices belong to BSbS, which is consistent with JCPDS #96-900-3467, thus further confirming the formation of B@B/CNH.

Carbon modification has the ability to narrow the band gap of nanomaterials, thus shifting their optical absorption towards the visible region, and eventually enhancing their

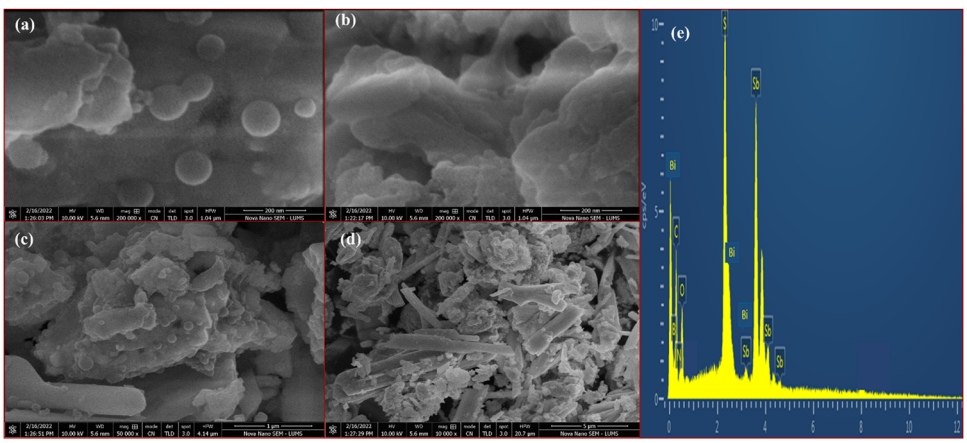

Fig. 3 SEM analysis of B@B/CNH nanocomposite (a) SEM analysis showing BSbS (b) SEM analysis showing BSbO (c) SEM analysis showing deposition of BSbS over CNH and BSbO (d) SEM image showing all morphologies and (e) EDX spectrum of B@B/CNH nanocomposite.

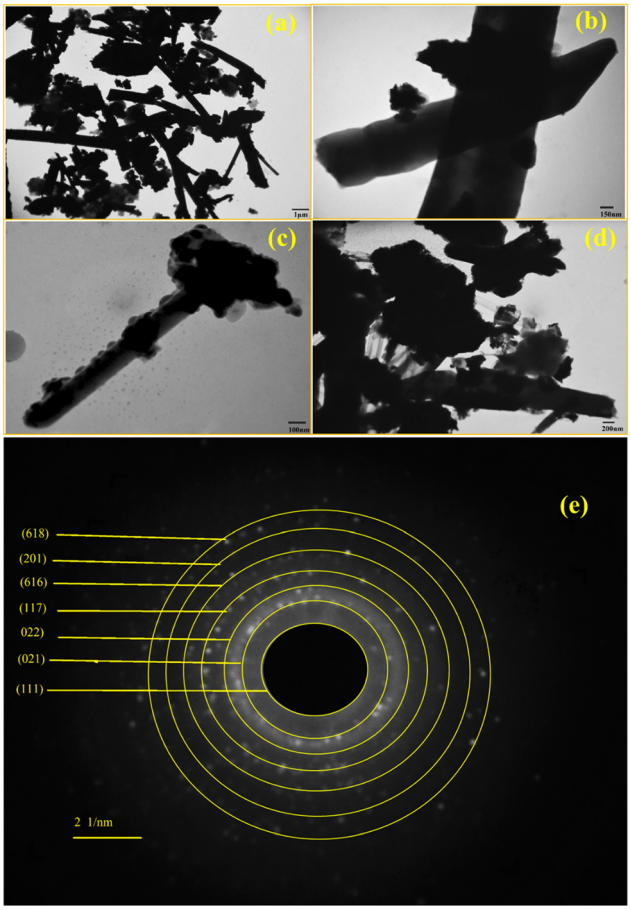

Fig. 4 (a)–(d) TEM micrographs of B@B/CNH nanocomposite at different resolutions (e) *hkl* indexing *via* SAED TEM image of B@B/CNH.

photocatalytic activity under visible light irradiation.[35] Thus, in the present study, CNH as a modifier also has the ability to narrow the band gap of BSbO from 2.73 eV to 2.65 eV in BSbO/CNH (Fig. S4, ESI†). Heterojunction assemblies can also play a crucial role in decreasing the band gap of B@B/CNH by combining different materials with complementary properties. The interaction between the different materials in heterojunctions has the capability to alter their electronic structure, thus creating a more efficient system for light absorption and charge separation, ultimately decreasing the band gap of nanocomposites. In this context, BSbS with a band gap of 2.69 eV (Fig. S4, ESI†) in the heterojunction assembly also contributed to decreasing the band gap of B@B/CNH (2.64 eV) (Fig. 5(a)). The band gap in a metal oxide/metal sulphide heterostructure assemblies has been found to be reduced due to ion exchange, leading to efficient transport properties in the nanocomposite, which can be valid in the present case due to the presence of BSbO/BSbS in B@B/CNH and BSbS was found to be coated over both BSbO and CNH *via* the XRD, SEM and TEM analysis.[36] The Tauc plot was used to calculate the band gap of B@B/CNH (2.64 eV), which was less than the band gap of BSbO/CNH (2.65 eV), BSbS (2.69 eV) and BiSbO (2.73 eV). Surface plasmon resonance is also considered to be responsible for the reduction in band gap in the case of the integration of CNH and BSbS, which pushes their adsorption edge toward a longer wavelength. This can be linked to the enhanced conductivity of B@B/CNH, where CNH act as an electron acceptor.[37,38] This fact was confirmed further by the electrochemical studies.

Heterojunctions play a crucial role in modulating the PL properties in various optoelectronic applications. Studies on different heterojunctions revealed the significant enhancement in their PL intensity and shifts in their emission peaks.[39] This is why the heterojunction synthesis was proposed in this work to obtain efficient luminescence, and eventually better photocatalysis. The Gaussian line-broadening mechanism was employed to evaluate the PL of B@B/CNH at the 350 nm excitation line (Fig. 5(b)). Its PL spectrum consisted of a violet component and blue component, and in the blue-violet emission, the blue emission with the maximum at 469 nm indicated the presence of a highly ordered structure, while the violet emission indicated the presence of metal vacancies or interstitials. The blue emission showed electron hopping from the conduction band to metal vacancy,[40] which is due to BSbO and BSbS. The blue PL band was found to correlate with the infrared absorption in relation to bonded oxygen, suggesting a connection between the blue PL intensity and oxygen due to the presence of BSbO[41] (Fig. S5, ESI†). The violet emission represents the electron hopping from the interstitial defect level to the metal vacancy,[40] which indicates the hopping of electrons from CNH to BSbO given that this peak belongs to BSbO/CNH (Fig. S5, ESI†).

FT-IR analysis was performed to assess the bonding nature and functional groups in B@B/CNH (Fig. 5(c)). The presence of BSbS was confirmed *via* inorganic–sulfide bonding peak at 1007 cm^{-1}.[42] Moreover, in the metal–sulphur bonding range of 600–400 cm^{-1}, the peak at 642 cm^{-1} corresponds to the symmetric-bending-vibration of metal–S, confirming the presence of BSbS.[43] The metal–oxygen bonding range was also found to be 600–400 cm^{-1}, and thus the peak at 642 cm^{-1} can be ascribed to BSbO, corresponding to the stretching vibration of the metal–O bond.[44] The FT-IR peaks at 1224 cm^{-1} and 832 cm^{-1} indicate the presence of CNH, given that these peaks belong to the C–C bonds. The band at 1224 cm^{-1} can be linked to the delocalization of the π-electron cloud in the CNH network.[45] Therefore, the presence of stretching and bending bands of M–O, M–S and C–C in the FT-IR spectrum of B@B/CNH validated its formation.

The surface area and porosity of B@B/CNH were calculated by Brunauer–Emmett–Teller (BET) analysis. The BET method is suitable for the surface area analysis of a variety of solid matrices. As shown in Fig. 5(d), the BET analysis was accomplished using the N_2 adsorption–desorption method on the surface of B@B/CNH. The BET analysis showed that the adsorption–desorption was according to the type V isotherm, indicating that adsorption may be challenging, which suggests that compared to adsorption, photocatalysis can be more advantageous because of the difficult recovery of the adsorbate.[46,47] The pore volume, surface area and pore diameter of B@B/CNH were calculated using BET analysis, which

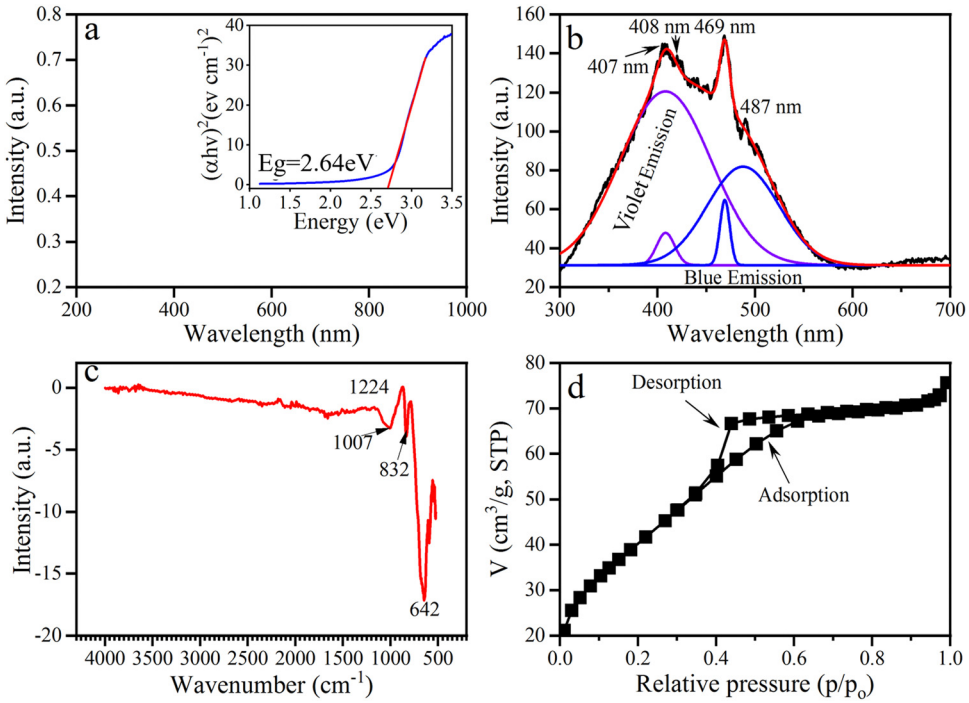

Fig. 5 Characterization of B@B/CNH nanocomposite, (a) UV-vis study and band gap, (b) PL study, (c) FT-IR analysis, and (d) BET study.

were 0.1166 $cm^3\ g^{-1}$, 149.45 $m^2\ g^{-1}$, and 3.1212 nm, respectively. The good surface area can be ascribed to the hybridization of CNH in the nanocomposite and its good porosity is ascribed to the deposition of BSbS on BSbO and CNH, which can also be the reason for the increase in surface area due to the high sorption of N_2 into its pores. Moreover, the adoption of vigorous stirring during the deposition of BSbS produced an intercalated exfoliated structure, which can lead to an enhanced surface area.

3.2 Optimization of the parameters for 5-CP degradation

It is a general observation that photocatalysts exhibit their full potential under the optimized condition. pH in relation to point of zero charge (ZPC) is considered essential to evaluate the ionization behavior on the surface of photocatalysts. The solid addition method was used to measure the pH_{ZPC} of B@B/CNH (Fig. 6(a)). For this measurement, 40 mL of 0.1 M potassium nitrate solution with varying initial pH was utilized in the pH range of 3–13. After that, B@B/CNH (0.1 g) was added to

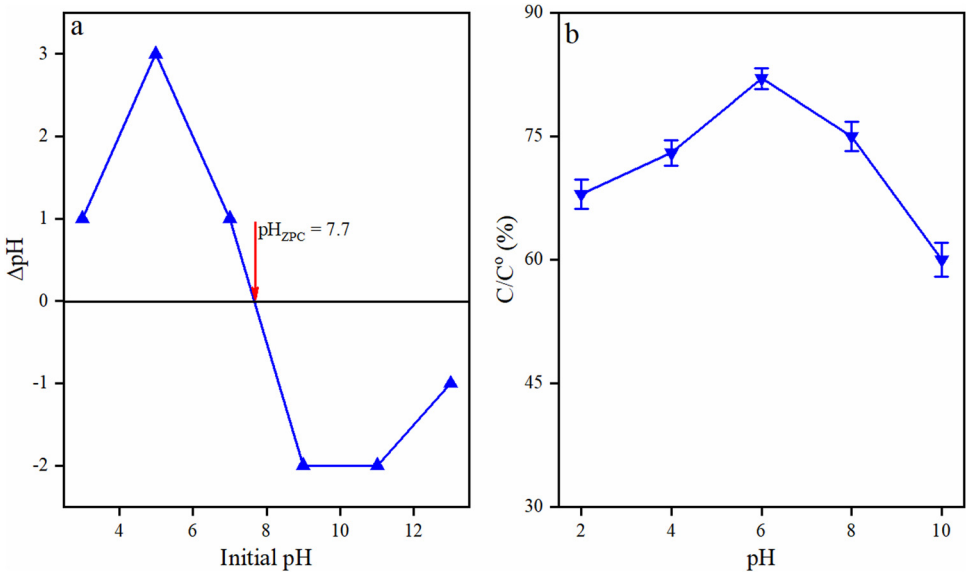

Fig. 6 (a) ZPC measurement for B@B/CNH and (b) effect of pH on the degradation of 5-CP by B@B/CNH.

each flask with varying pH and shaken for 24 h at 30 °C, and then the final pH was measured. As seen in Fig. 6(a), the pH_{ZPC} of B@B/CNH was measured to be 7.7. The surface of a photocatalyst is positively charged at a pH less than pH_{ZPC} and *vice versa*. Thus, in accordance with the pH_{ZPC} study, the surface of B@B/CNH will attain a negative charge at pH > 7.7 (basic) and positive charge at pH < 7.7 (acidic). The effect of pH on the degradation of 5-CP was evaluated using the photocatalyst dose of 0.01 g L^{-1}, 5-CP concentration of 10 ppm and visible light irradiation of 120 min in the pH range of 2–10. The maximum 5-CP degradation was seen at pH 6 compared to extreme acidic or basic pH. The degradation percentages were 68%, 73%, 82%, 75% and 60%, when the pH was 2, 4, 6, 8 and 10, respectively (Fig. 6(b)). Here, molecules of 5-CP were adsorbed electrostatically on the positively charged surface of B@B/CNH (pH < pH_{ZPC}), and subsequently degraded. The results showed that the degradation of 5-CP increased with an increase in pH until it reached the optimum pH, and then it started decreasing. Additionally, compared with the efficiency of BSbO, BSbO, and BSbO/CNH, it was observed that B@B/CNH showed superior degradation towards 5-CP (Fig. S6a, ESI†). The degradation efficiency followed the order of B@B/CNH (82%) > BSbO/CNH (79%) > BSbS (75%) > BSbO (72%). There is the possibility of the greater production of hydroxyl radicals at acidic pH due to the interaction of holes with hydroxide ions.[48] Finally, this suppressed the recombination of charged species, increasing the rate of degradation of 5-CP. This assumption was further confirmed by the scavenger and DFT studies. Both polar and non-polar interactions can exist between the photocatalyst (B@B/CNH) and pollutant (5-CP).[49]

The optimum dosage of B@B/CNH was determined to be pH 6 using 10 ppm 5-CP and 120-min irradiation time after varying the dosage in the range of 0.02–0.4 g L^{-1}. As the dosage of B@B/CNH increased, the degradation of 5-CP increased, and to achieve 87% degradation of 5-CP, the optimum dosage of B@B/CNH was 0.1 g L^{-1} (Fig. S6b, ESI†). After that, no significant increase in degradation was observed when the dosage was increased to 0.4 g L^{-1}. In the case of BSbO, the highest degradation of 5-CP was observed at a dosage of 0.18 g L^{-1}, whereas BSbS and BSbO/CNH showed the maximum 5-CP degradation at a dosage of 0.14 g L^{-1}. These results showed the greater degradation capability of B@B/CNH compared to its counterparts. Initially, the increase in 5-CP degradation with an increase in dosage may be the result of additional interaction sites on the photocatalyst surface, enabling the more effective absorption of visible light. Additionally, at greater dosage, the effective catalyst suspension was reduced, making it more difficult for light to disperse efficiently, and eventually reducing the amount of 5-CP that can be absorbed on the photocatalyst surface. Another hypothesis is that the active photocatalyst becomes inactive after interacting with the ground state, making it incapable of breaking down 5-CP.[50,51]

For the optimization of the 5-CP concentration, its concentration was varied in the range of 5–25 ppm and the other optimized conditions were kept constant. As seen in Fig. S6c (ESI†), the rate of degradation first increased as the 5-CP concentration increased, before becoming constant after the optimum concentration. At 10 ppm concentration of 5-CP, B@B/CNH showed the maximum degradation of 89% and a similar trend was also observed for BSbO, BSbS, and BSbO/CNH. Again, it can be observed that B@B/CNH performed much better in degrading 5-CP compared to BSbO, BSbS, and BSbO/CNH. The reduction in efficacy may be associated with the decrease in the amount of active radicals because 5-CP molecules could not be adsorbed onto the active sites. Another explanation is that an elevated concentration of 5-CP created superfluous reaction intermediates, which cling to the photocatalyst surface for extended periods. Thus, BSbO/CNH showed good efficiency to degrade 5-CP under the optimized parameters, which was relatively higher compared to BSbO and BSbS (Fig. S6c, ESI†).

3.3 Kinetic study

A kinetic study was performed to evaluate the degradation behavior of 5-CP by B@B/CNH, BSbO/CNH, BSbS and BSbO *via* the Langmuir–Hinshelwood model. This work demonstrated that pseudo-first-order kinetics governed the degradation of 5-CP in the presence of visible light. The molecules of 5-CP were adsorbed on the surface of the photocatalysts prior to the bimolecular reaction. Therefore, the adsorption of photons and 5-CP onto surface of photocatalysts regulated the rate of photocatalysis. Pseudo-first-order kinetics were followed here, in which $\ln(C_t/C_0)$ was plotted against time (Fig. 7(a)). The values of $\ln(C_t/C_0)$ were found to decrease linearly due to the increase in free radicals with an increase in the irradiation period. Given that the photocatalytic process is primarily dependent on the duration of visible light irradiation, we computed K_{app} in this case as a function of visible light irradiation time using eqn (1). The slopes were used to calculate the values of K_{app} (apparent rate constant).

$$\ln \frac{C_t}{C_0} = K_{app} t \quad (1)$$

where C_0 is the initial concentration of 5-CP and C_t is the concentration of 5-CP at the related time during the degradation of 5-CP.

The kinetic study can help compare the effect of the heterojunction assembly and CNH modification on the activity of the photocatalyst for the degradation of 5-CP. K_{app} was observed to be −0.0129, −0.0148, −0.0185 and −0.0240 and R^2 was 0.972, 0.976, 0.985 and 0.975 for BSbO, BSbS, BSbO/CNH, and B@B/CNH, respectively. Under the optimum conditions, the degradation percentage was 81%, 82%, 84% and 93% for BSbO, BSbS, BSbO/CNH, and B@B/CNH, respectively (Fig. 7(a)), (Table S2, ESI†). These observations confirmed the fact that the heterojunction assembly and modification by carbon materials increased the efficacy of the photocatalyst. Metal sulfides have shown promising photocatalytic activity compared to metal oxides due to their lower band gap and efficient response to light, making them suitable for solar-driven reactions.[52,53] Metal oxides have been used commonly due to their stability and eco-friendly nature, while also exhibiting a better response

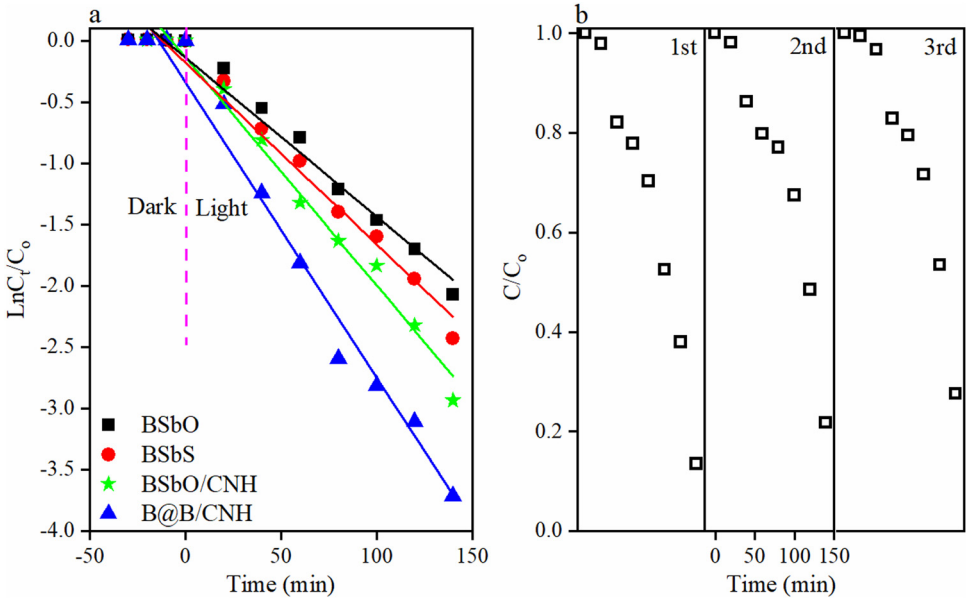

Fig. 7 (a) Kinetic study of BSbO, BSbS, BSbO/CNH, and B@B/CNH and (b) recycling study of B@B/CNH nanocomposite.

to ultraviolet light, whereas metal sulfides have a lower band gap and respond well to visible light, making them more efficient in photocatalytic applications.[53] Thus, in this work, BSbS was deposited over the heterojunction assembly of the BSbO/CNH composite and the developed B@B/CNH material showed much greater activity compared to its counterparts. 5-CP is degraded by capturing holes and their conversion into reactive radical species on the photocatalyst surface. This process can be compromised if holes recombine with electrons before the photocatalyst can capture them, which is a significant disadvantage in any photocatalyst. In the current study, our focus was on the inhibition of charge carrier recombination, and thus this nanocomposite was designed, in which carbon modification and the heterojunction have the capability to lessen the recombination of charge carriers. The introduction of an organic–inorganic hybrid heterojunction at the interface established a p–n junction with a built-in electric field, which effectively separated the photo-generated charge carriers, leading to a significantly increased photocurrent and improved photocatalytic performance.[54] CNH is credited to improving the performance of BSbO by acting as the active site, which increased its electrical conductivity and adsorption capacity. It is believed that the superior electronic conductivity of CNH causes the photo-excited electrons to be quickly captured by CNH and transferred to the BSbS@BSbO composite, thus suppressing the recombination of charge carriers.[55] Therefore, B@B/CNH can be the ideal material for the degradation of 5-CP and other similar pollutants due to the synergistic impact of photocatalysis and adsorption.

3.4 Recycling ability of B@B/CNH

Three consecutive cycles were performed to check the recycling capacity of B@B/CNH. Fig. 7(b) depicts the 5-CP degradation cycles in sequential order. In this instance, 5-CP was exposed to visible light at room temperature under the optimum reaction conditions after adding B@B/CNH. After the degradation experiment, centrifugation was performed to clean and recycle the used photocatalyst using water and ethanol. Three cycles of photocatalysis were performed, yielding degradation rates of 93%, 87%, and 86% for the 1st, 2nd and 3rd cycle, respectively (Fig. 7(b)). The slow decline in efficiency can be attributed to the accumulation of side products on the active sites of B@B/CNH. Even after three rounds, the photocatalytic activity was still fairly high. This demonstrates the endurance of B@B/CNH, which was more likely caused by CNH given that CNH can increase the mechanical strength and stability of catalysts.

3.5 Comparative analysis of the efficiency of B@B/CNH with reported catalysts

A comparative study was performed to check the efficiency of the prepared B@B/CNH (Table 1). B@B/CNH was relatively efficient compared to many reported catalysts and only Ag/anatase TiO_2 nanotubes and α-Fe_2O_3/ZnO composites showed higher degradation than B@B/CNH of 99% and 100%, respectively. However, it should be noted that a high dosage of 1 g L^{-1} of Ag/anatase TiO_2 nanotubes and a greater irradiation time of 180 min were utilized, and further silver-based photocatalysts are expensive to synthesize at the commercial level.[31] Similarly, a high dosage of 1.5 g L^{-1} and 240-min irradiation time were applied in the case of α-Fe_2O_3/ZnO composites. Alternatively, B@B/CNH showed 93% degradation with a dosage of only 0.1 g L^{-1} in 140 min using 10 ppm of 5-CP.

3.6 Effect of different pollutants and scavengers

The degradation of 5-CP on B@B/CNH was tested in the presence of various supplementary phenolic pollutants to replicate real-world industrial effluent. The four contaminants that were chosen are bisphenol A, 4-chlorophenol, pyro-catechol

Table 1 Comparative study of B@B/CNH with reported catalysts for the degradation of 5-CP

Photocatalyst	Dosage (g L^{-1})	5-CP (ppm)	Time (min)	Degradation (%)	Ref.
Ag/Anatase TiO_2 nanotubes	1	10	180	99	31
Bi/SnO_2/TiO_2-graphene	0.3	20	120	84	28
Mont TiO_2	2.5	10	200	78	29
Mont Bi/TiO_2	2.5	10	200	84	29
$FeNi_3$/SiO_2/ZnO	0.5	10	180	100	30
NiO coupled $NiTiO_3$	—	—	360	66	56
α-Fe_2O_3/ZnO composites	1.5	10	240	100	57
B@B/CNH	0.1	10	140	93	This work

and Acid Red-88 dye. The spectral results are presented in Fig. S7a (ESI†), which showed the exposure of the mixtures (5-CP/other pollutant) to visible light irradiation at 300 nm. In the presence of these pollutants, the degradation efficacy of 5-CP on B@B/CNH was computed, as illustrated in Fig. 8(a). All the tested contaminants had had an impact on the degradation of 5-CP, which lowered its degradation efficacy. In the presence of bisphenol A, 4-chlorophenol, pyro-catechol and Acid Red-88 dye, the degradation percentage of 5-CP was found to be 25%, 30%, 38%, and 79%, respectively (Fig. 8(a)). The best degradation of 5-CP (93%) without other pollutants indicated that B@B/CNH was not selective towards the degradation of 5-CP. However, this advantage of B@B/CNH can be used to remove/degrade various other pollutants and phenolic compounds in addition to 5-CP.

The scavenger study was performed to determine the role of free radicals and their possible contribution towards the photocatalysis of 5-CP by B@B/CNH. Four scavengers including ascorbic acid (AA), isopropyl alcohol (IPA), potassium dichromate ($K_2Cr_2O_7$), and disodium ethylene diamine tetraacetate (EDTA-2Na), which scavenge superoxide radicals, hydroxyl ions, electrons, and holes, respectively, were applied. The scavenger solution was poured into a 5-CP solution and exposed to visible light for 140 min. The photocatalytic degradation was observed to decrease in the order of no scavenger > $K_2Cr_2O_7$ > EDTA > IPA > AA (Fig. 8(b)), (Fig. S7b, ESI†). These findings demonstrate that AA was responsible for the greatest reduction in photocatalysis, indicating the active involvement of superoxide radicals in the photocatalytic degradation of 5-CP by B@B/CNH. IPA also played a significant role in decreasing the degradation of 5-CP, thus indicating that hydroxyl radicals also contributed significantly to the degradation of 5-CP.

3.7 DFT study

The mechanism for the photodegradation of 5-CP was estimated using DFT. The B3LYP-D3 (BJ) level exchange–correlation functional having the def2-tzvp basis set based on ORCA 5.0.3 was used to optimize the geometry and compute the excited state. To ensure that there were no imaginary frequencies in the stable configuration, frequency calculations were performed. To account for the effects of water given that the 5-CP solution was an aqueous solution, the SMD model, which is a continuum solvation model, was employed. It is based on the quantum mechanical charge density of a solute molecule interacting with a continuum description of the solvent.

VMD 1.9.3 was used to view all the structures and isosurfaces. An essential idea in conceptual density functional theory (also known as CDFT) is the Fukui function. CDFT has been extensively applied to forecast the regioselectivity of electrophilic, nucleophilic, and radical attacks. Thus, Multiwfn 3.8 at the B3LYP/6-31G(d) level was employed to compute the condensed Fukui functions of nucleophilic ($f+$), electrophilic ($f-$), radical attack ($f0$), Hirshfeld charges and condensed dual descriptors (CDD) as well as the HOMO, LUMO, and surface electrostatic potential (ESP) of 2-MBT. VMD (1.9.3 version) was used to draw $f+$, $f-$, $f0$, CDD, HOMO and LUMO, *etc.* (Fig. 9). Eqn (2) defines the Fukui function in specific terms.

$$f(r) = \left[\frac{\partial \mu}{\partial v(r)}\right]_N = \left[\frac{\partial \rho(r)}{\partial N}\right]_{v(r)} \quad (2)$$

where N is the number of electrons, $\rho(r)$ represents the electron density at location r in space, and the external potential is represented by the constant term "v" in the partial derivative. One can compute the CDD, $f+$, $f-$ and $f0$ as follows:

$$\text{Nucleophilic attack: } f_A^+ = q_N^A - q_{N+1}^A$$

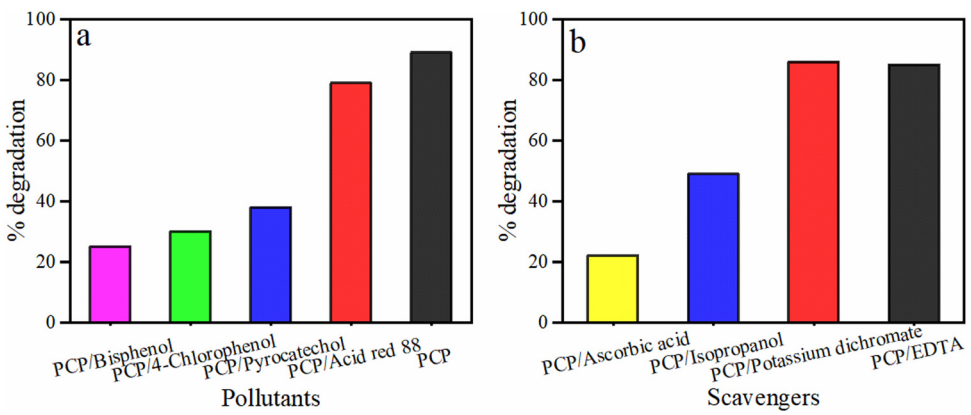

Fig. 8 Effect of (a) different pollutants and (b) scavengers on the degradation efficiency of 5-CP by B@B/CNH nanocomposite.

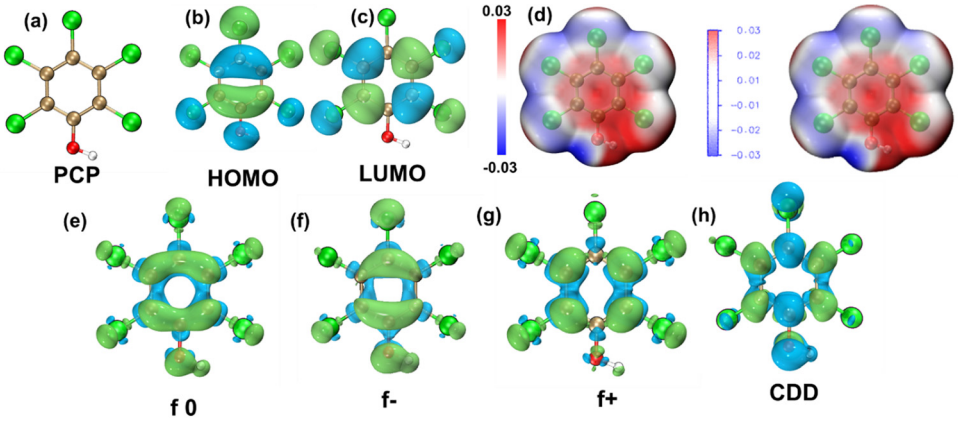

Fig. 9 (a) 5-CP chemical structure, (b), (c) distribution of HOMO and LUMO orbitals on 5-CP, (d) 5-CP ESP mapping, (e)–(g) condensed Fukui functions, and (h) condensed dual descriptors.

$$\text{Electrophilic attack: } f_{\mathrm{A}}^{-} = q_{N-1}^{\mathrm{A}} - q_{N}^{\mathrm{A}}$$

$$\text{Radical attack: } f_{\mathrm{A}}^{0} = (q_{N-1}^{\mathrm{A}} - q_{N+1}^{\mathrm{A}})/2$$

In the condensed dual descriptor (CDD), the charge of atom A is represented by the symbol q^{A}. This analysis showed that the pollutant (5-CP) atoms such as Cl11, O7, and Cl9 have negatively charged surfaces, which suggests that they are most likely to play a role in the breakdown of 5-CP. Hirshfeld charges and the Fukui index ($f0$, $f+$, and $f-$) were used to examine the nucleophilic, electrophilic and radical attacks on the atoms of 5-CP, respectively (Fig. 9). This investigation demonstrated the nucleophilicity of the oxide radicals and electrophilicity of holes.

High values of $f0$, $f+$, and $f-$ indicate that an atom is very vulnerable to attack in the order of oxide radical > hydroxyl radical > electrons > holes (same tendency showed by scavenger study). However, the accurate identification of the reaction sites is still difficult. As a result, to identify the reaction sites, we employed the condensed dual descriptor (CDD). The 5-CP atoms C2, C5, Cl11, Cl13, and O7 exhibited clear nucleophilicity, whereas the 5-CP atoms C3, C4, C6, Cl9, and Cl12 exhibited marked electrophilicity. Given that Cl 9 is in an orthogonal position to hydroxyl substituents, it has the most active electrophilic sites for attacking holes and hydroxyl radicals, respectively. The intermediate reaction sites were seen to vary as a result of continuous structural alterations. The Fukui function examines these structural alterations in intermediates (Table S3, ESI†). Among the atoms, C1 and Cl10 have comparatively positive CDD values, indicating their high vulnerability toward oxide radical attack and subsequent C–Cl bond breaking. The HUMO–LUMO gap is 5.29 eV with orbital 65 being HOMO (−6.67 eV) and orbital 66 being LUMO (−1.37 eV).

3.8 Electrochemical study

Galvanostatic charge discharge (GCD) and cyclic voltammetry (CV) were used to validate the suitability of B@B/CNH for supercapacitor applications and the results are shown in Fig. S8 and S9 (ESI†). As shown in Fig. S8a (ESI†), the CV curve was reversible, which is due to the capacity of B@B/CNH to store charge and subsequent creation of an electric double layer at the electrode surface in the potential window of 0.2–0.85 V. An increase in the cathodic and anodic currents was detected with an increase in the scan rate at all the examined scan rates. However, BSbS showed quasi-reversible behavior when the scan rate reached 100 mV s^{-1} (Fig. S8b, ESI†), whereas BSbO showed almost irreversible behavior at a high scan rate (Fig. S8c, ESI†). This indicates the existence of a reversible electrochemical reaction at the interface (electrode/electrolyte) and high storage capacity of B@B/CNH in comparison to its counterparts. The GCD analysis was completed by varying the current density in the range of 1–16 A g^{-1} (Fig. S9a, ESI†). Linear charge and discharge behavior were seen at all current densities, indicating a 100% charge to discharge ratio with no internal resistance (IR) drop.[58] This behavior indicates the effective electronic conducting qualities of B@B/CNH. A similar and relatively less charge to discharge ratio was observed for BSbS (Fig. S9b, ESI†) and BSbO (Fig. S9c, ESI†).

The capacitance and rate capability were estimated using eqn (3).

$$C_{\mathrm{s}} = \frac{I\Delta t}{\Delta V} \tag{3}$$

where C_{s} is the specific capacity, Δt is the discharge time, I is the current density, and ΔV is the working potential window. At a current density of 8 A g^{-1}, the specific capacitance of B@B/CNH was 97.43 F g^{-1}, which is higher compared that of to BSbS (90.47 F g^{-1}) and BSbO (83.50 F g^{-1}), as shown in Fig. 10(a). B@B/CNH possesses three types of morphologies, which according to the literature, do not impact the specific capacitance, whereas it affects the interaction between the composite surface and water layer at the surface. The good value of the specific capacitance of B@B/CNH indicates the good interaction between the composite and water layer on its surface due to its high surface area. Ion buildup on the surface of the composite and water chemisorption can be facilitated by strong interaction between the water layer and composite. B@B/CNH exhibited good interaction due to its high surface

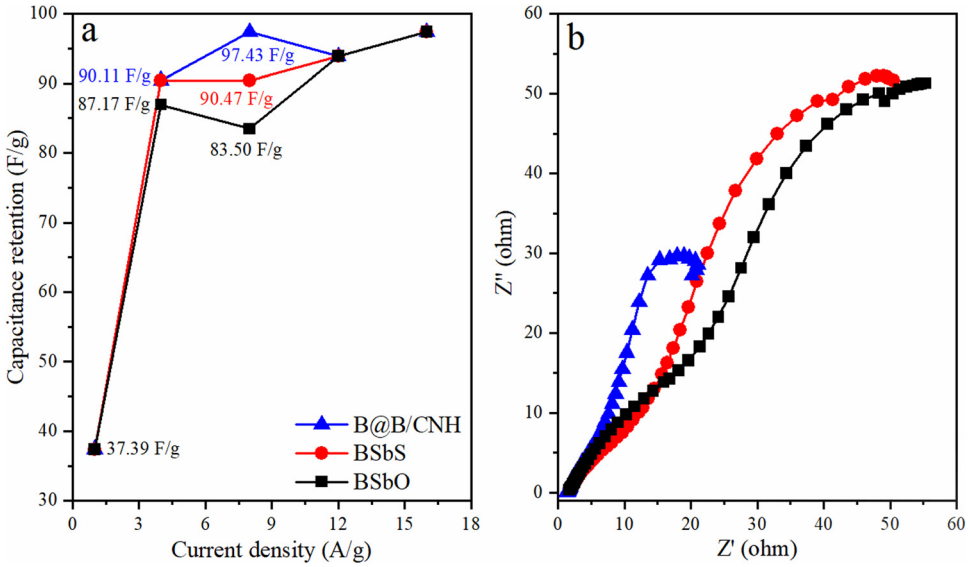

Fig. 10 Electrochemical study (a) graph of current density *vs.* capacitance retention for BSbO, BSbS, and B@B/CNH (b) EIS graphs with circuit for BSbO, BSbS, and B@B/CNH.

area compared to BSbO and BSbS. Therefore, optimizing the interaction between a solid and a solvent can result in better energy conversion and storage technologies.[59]

An electrochemical impedance spectroscopy (EIS) study was performed for B@B/CNH, which was conducted at an open circuit potential of 26 mV in the frequency range of 105 Hz and 0.1 Hz, as illustrated in Fig. 10(b). EIS can be used to determine the resistivity of catalysts and understand the kinetics of electron transport. The diameter of the semicircle in the EIS plot indicates the electron transfer kinetics.[60] As observed in Fig. 10(b), the diameter of the semicircle is small for all the composites, thus indicating fast electron transfer kinetics for BSbO, BSbS and B@B/CNH. The Nyquist plot of the EIS spectra displays the difference in impedance, $|Z|$, as a function of frequency. Concentration polarization can be responsible for the hindrance in mass transport, which can be predicted by the intercept, providing information about the resistance to mass transfer.[60] As observed in Fig. 10(b), the value of the intercept is zero, indicating the negligible hindrance in mass transport for B@B/CNH, BSbS and BSbO. According to the EIS plots, all the composites showed good electron transfer kinetics with negligible hindrance in mass transport.

3.9 Possible mechanism for the degradation of 5-CP

Some nanocomposites with different semiconductors have been combined in a *Z*-scheme heterojunction configuration to improve their redox capabilities, effective photo-carrier separation and efficient photocatalytic activities for the degradation of different organic contaminants.[61–64] In same context, this catalyst was designed specifically to follow an indirect *Z*-scheme given that it has two semiconductors (BiSbO and BiSbS) with a close band gap. According to the literature, metal oxides act as oxidative centers, whereas metal sulphides mostly act as reductive centers in photocatalysis.[65] Metal sulfides are better light absorbers, and thus they are more prone to photocorrosion, particularly in an oxidative environment, making them suitable for reductive processes.[66–68] Moreover, experiments comparing the poisoning effects of oxides and sulphides on conduction suggested that sulphur has a greater poisoning effect, thus indicating its greater potential for electron capture compared to oxides.[69] Conversely, oxides tend to be more stable under various conditions, which can be advantageous in certain photocatalytic applications for transferring electrons.[67,70] CNH is coordinated because it has the ability to capture electrons and transmit to BSbS due to the higher electronegativity of sulphides compared to CNH.[55]

The potential mechanism for the degradation of 5-CP by B@B/CNH was predicted based on the scavenger and DFT studies in relation to active radicals (Fig. 8(b)). According to the scavenger and DFT studies, oxide radicals are active radicals to degrade 5-CP. The band gap analysis revealed that BSbS significantly narrowed the band gap. Theoretical calculations were applied to calculate the valence band and conduction band edges of BSbO and BSbS in B@B/CNH using the Mulliken electronegativity and band gap values (eqn (4)–(6)), respectively.[71]

$$E_{VB} = X - E_e + 0.5E_g \quad (4)$$

$$E_{CB} = E_{VB} - E_g \quad (5)$$

$$E_g = E_{VB} - E_{CB} \quad (6)$$

where E_{VB} represents the energy in relation to the valence band and E_{CB} represents the energy in relation to the conduction band. E_g represents the band gap energy and E_e represents the energy of free electrons, which is 4.5 eV *vs.* NHE.[71,72] X represents the geometric mean of the Mulliken electronegativity of the constituent atoms in the semiconductor. The arithmetic means of the first electron affinity and the first ionization

energy determines the Mullin electronegativity of an atom. According to the calculations, the X values of BSbO and BSbS were found to be 8.24 eV and 7.19 eV, respectively. The E_{VB} of BSbO and BSbS were calculated to be 3.99 and 3.94 eV, respectively. The reported valence band of BSbO is 3.2 eV, which is close to the calculated valence band.[73] The E_{CB} of BSbO and BSbS was calculated to be 1.21 and 0.75, respectively (Fig. 12). To assume the direction of electron transfer and charge redistribution, the work function (Φ) of BSbO and BSbS was calculated using ultraviolet photoelectron spectroscopy (UPS) analysis (eqn (7)–(9)).[74,75]

$$\Phi = 21.22 - (E_{cutoff} - E_F) \quad (7)$$

$$E_F = E_{cutoff} - 21.22 \quad (8)$$

$$E_F = -\Phi \quad (9)$$

where E_F is the Fermi level, which was calculated by using the photo energy of the radiation source of HeI (21.22 eV) and E_{cutoff}. E_{cutoff} is the cutoff energy at which the kinetic energy of electrons becomes zero and the intensity also drops to zero, as shown in Fig. 11(a). The E_{cutoff} of BSbO and BSbS is 18.12 and 18.99 3 V, respectively. E_F is −3.1 and −2.23 eV for BSbO and BSbS, respectively (eqn (8)), which implies that an e from BSbS could spontaneously diffuse into BSbO *via* CNH upon their successful hybridization, leading to the creation of an IEF from BSbS to BSbO. The work function (Φ) is the photon energy minus the binding energy (E_{cutoff}) when the Fermi level is set to zero (eqn (7)). Φ was determined to be 3.1 and 2.23 for BSbO and BSbS, respectively, according to eqn (9). In this context, given that BSbO has a lower E_F compared to BSbS, electrons will migrate from BSbS to BSbO to make E_F reach equilibrium after hybridization, thus leading to the formation of a depletion layer in BSbS and electron accumulation layer in BSbO.

Under visible light irradiation, both BSbS and BSbO were photoexcited to create electron–hole pairs (Fig. 12). In this scheme (Fig. 12), the migration of electrons was shown from the conduction band of BSbS (PS-II) to the valence band of BSbO (PS-I), which limited the recombination of charge carriers. The *Z*-scheme maintained strong oxidation in PS-II and strong reduction in PS-I by combining migrating electrons with holes in the valence band of PS-I. Furthermore, CNH can function as a bridge between the two BSbO and BSbS because CNH has the ability to capture electrons and transmit to BSbO due to the higher electronegativity of the oxide than CNH. In addition, CNH (an electron mediator) can also create oxide radicals from oxygen and CNH was credited to improve the performance of BSbO by providing active sites, which increased the electrical conductivity and adsorption capacity. It was believed that the superior electronic conductivity of CNH can be linked to the quick capture of photo-excited electrons, followed by photo-excited electron transfer to BSbS@BSbO, thus suppressing the recombination of charge carriers.[55] The presence of oxygen vacancies in BSbO can create inter-band gap states below its conduction band, thus increasing the lifetime of photoelectrons by trapping electrons inside the deep defected sites.[76] The increased surface area due to the heterojunction assembly was also considered responsible for the increased charge separation and its transportation. This is because the introduction of an organic–inorganic hybrid heterojunction at the interface establishes a p–n junction with a built-in electric field, which effectively separates photo-generated charge carriers, leading to a significant increase in photocurrent and improved photocatalytic performance.[54]

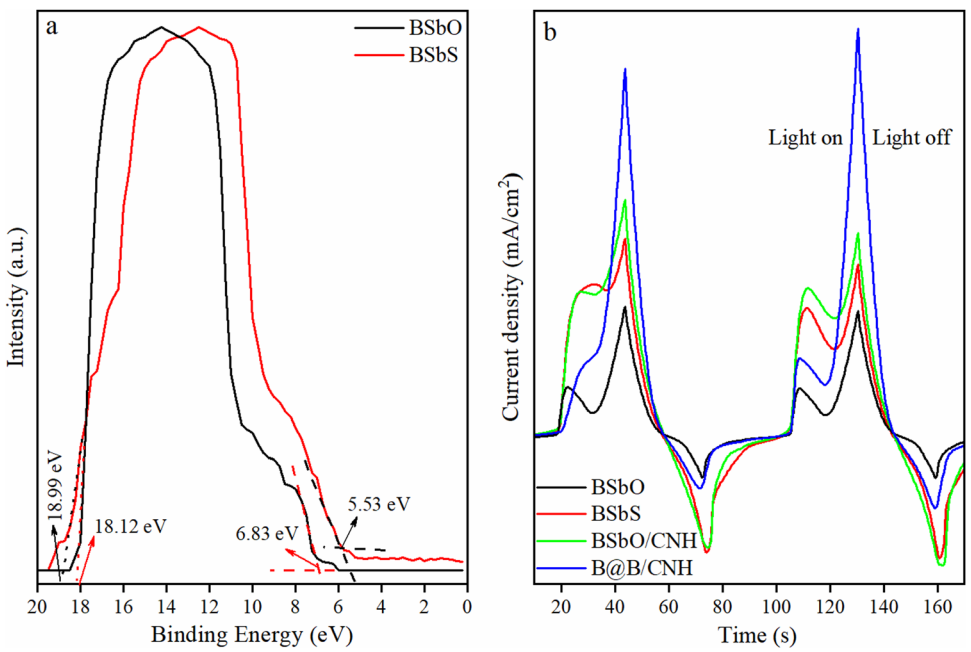

Fig. 11 (a) UPS spectrum of BSbO and BSbS and (b) current density vs time for BSbO, BSbS, BSbO/CNH and B@B/CNH.

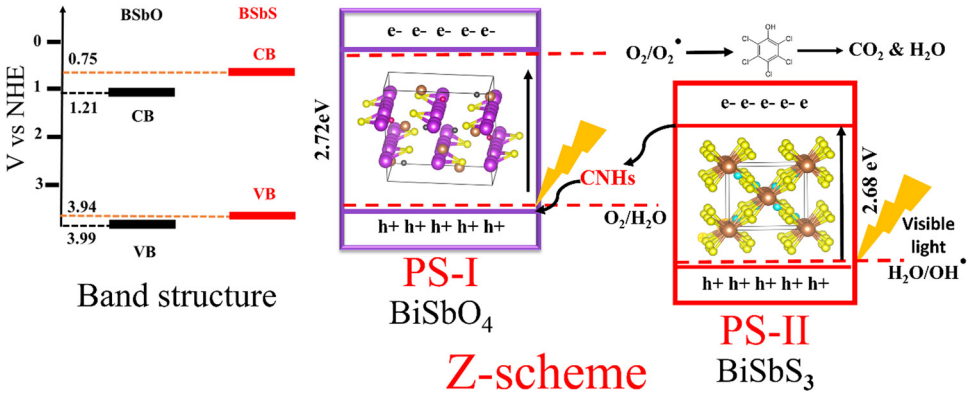

Fig. 12 Mechanism for the degradation of 5-CP by B@B/CNH nanocomposite.

To understand the effectiveness of the electron/hole separation process, the photo-electrochemical behaviors of the samples were observed by the transient photocurrent response (TPR), and the formation (light on) and dissolution (light off) kinetics of the charge carriers in BSbO, BSbS, BSbO/CNH and B@B/CNH are shown in Fig. 11(b). The higher transient current intensity induce the creation and separation of holes and electrons.[77] B@B/CNH exhibited a significantly higher current intensity compared to BSbO, BSbS and BSbO/CNH (Fig. 11(b)), thus indicating the advantage of efficient e–h pair separation. According to Fig. 11(b), BSbO/CNH also showed efficient charge carrier separation, followed by BSbS, and the least effective was BSbO, thus indicting the effective role of CNH in separation of charge carriers. The mechanism in the context of electrochemical studies was observed *via* the calculation of the current density and EIS study (Fig. 11(b) and (b), respectively). The impressive current density of B@B/CNH indicated the efficient separation and movement of charge carriers, thus strengthening our claim of creating a photocatalyst showing less charge carrier recombination. The EIS studies further confirmed the efficient charge transfer with less resistance *via* B@B/CNH. This section elaborates the possible mechanism for the degradation of 5-CP by B@B/CNH and achievement of the goal of an efficient photocatalyst with less charge recombination.

4. Conclusions

This work was designed to degrade 5-CP, which is an endocrine disruptor with serious consequences on human health. In this study, a simple and reliable method was used to synthesize B@B/CNH. When B@B/CNH was examined for the degradation of 5-CP, it discovered to be the most effective in comparison to its counterparts due to its ability to inhibit charge carrier recombination effectively. According to the scavenger study, it was found that oxide radicals played the most significant role in the degradation of 5-CP compared to hydroxyl radicals, electrons and holes. B@B/CNH was found to be a significant material for wastewater treatment due to its ability to simultaneously degrade other phenolic compounds, and given that B@B/CNH was found to be less selective for 5-CP breakdown in the presence of other phenolic compounds. The degradation behavior of 5-CP on B@B/CNH was observed using DFT calculations, which revealed that the chlorine group with high electron density at the *ortho* position to the hydroxyl group was more susceptible to attack by electrophiles. Furthermore, electrochemical studies were executed to assess the electronic properties of B@B/CNH. The heterojunction assembly of B@B/CNH was found to be responsible for the efficient conductivity, while the high surface area due to CNH and BSbS was responsible for the excellent specific capacitance.

Author contributions

Maria Batool: methodology, writing – original draft, formal analysis, investigation, data curation. Muhammad Nadeem Zafar: project administration, supervision, conceptualization, writing – review & editing.

Data availability

The authors confirm that the data supporting the findings of this study are available within the article and its ESI.†

Conflicts of interest

The authors have no conflicts of interest to declare that are relevant to the content of this study.

Acknowledgements

The authors acknowledge the Department of Chemistry, University of Gujrat, Gujrat, Pakistan for providing the facilities to accomplish the present research work. We are grateful for financial support from Chinese Academy of Sciences (CAS) President's International Fellowship Initiative (PIFI) program for Visiting Scientists (grant no. 2024PVB0003). MNZ acknowledges the CAS for the grant of "President's International Fellowship Initiative (PIFI)" award.

References

1 R. McKinlay, J. Plant, J. Bell and N. Voulvoulis, Endocrine disrupting pesticides: implications for risk assessment, *Environ. Int.*, 2008, **34**, 168–183.

2 W. Mnif, A. I. H. Hassine, A. Bouaziz, A. Bartegi, O. Thomas and B. Roig, Effect of endocrine disruptor pesticides: a review, *Int. J. Environ. Res. Public Health*, 2011, **8**, 2265–2303.

3 N. Abdullah, N. Yusof, W. Lau, J. Jaafar and A. Ismail, Recent trends of heavy metal removal from water/wastewater by membrane technologies, *J. Ind. Eng. Chem.*, 2019, **76**, 17–38.

4 X. Zhang, P. Gu and Y. Liu, Decontamination of radioactive wastewater: State of the art and challenges forward, *Chemosphere*, 2019, **215**, 543–553.

5 M. N. Rashed, Adsorption technique for the removal of organic pollutants from water and wastewater, *Organic pollutants-monitoring, risk and treatment*, 2013, vol. 7, pp. 167–194.

6 K. A. M. Said, A. F. Ismail, Z. A. Karim, M. S. Abdullah and A. Hafeez, A review of technologies for the phenolic compounds recovery and phenol removal from wastewater, *Process Saf. Environ. Prot.*, 2021, **151**, 257–289.

7 T. Carswell and H. Nason, Properties and uses of pentachlorophenol, *Ind. Eng. Chem.*, 1938, **30**, 622–626.

8 G. Xiaoyan, Z. Xiaojie, T. Yincai, H. Yabei, Y. Zhang and Z. Yanqin, Preparation of Cu_2O/AC photocatalysts and their photocatalytic activity in degradation of pyrocatechol, *Kinet. Catal.*, 2011, **52**, 672–677.

9 A. Zada, Y. Qu, S. Ali, N. Sun, H. Lu, R. Yan, X. Zhang and L. Jing, Improved visible-light activities for degrading pollutants on TiO_2/g-C_3N_4 nanocomposites by decorating SPR Au nanoparticles and 2, 4-dichlorophenol decomposition path, *J. Hazard. Mater.*, 2018, **342**, 715–723.

10 L. C. Lei, Y. Zhang, X. W. Zhang, Y. X. Du, Q. Z. Dai and S. Han, Degradation performance of 4-chlorophenol as a typical organic pollutant by a pulsed high voltage discharge system, *Ind. Eng. Chem. Res.*, 2007, **46**, 5469–5477.

11 M. Mukhopadhyay and P. Chakraborty, Plasticizers and bisphenol A: Emerging organic pollutants along the lower stretch of River Ganga, north-east coast of the Bay of Bengal, *Environ. Pollut.*, 2021, **276**, 116697.

12 F. Orton, I. Lutz, W. Kloas and E. J. Routledge, Endocrine disrupting effects of herbicides and pentachlorophenol: in vitro and in vivo evidence, *Environ. Sci. Technol.*, 2009, **43**, 2144–2150.

13 K. A. McAllister, H. Lee and J. T. Trevors, Microbial degradation of pentachlorophenol, *Biodegradation*, 1996, **7**, 1–40.

14 J. Seiler, Pentachlorophenol, Mutation Research/Reviews in Genetic, *Toxicology*, 1991, **257**, 27–47.

15 W. Zheng, H. Yu, X. Wang and W. Qu, Systematic review of pentachlorophenol occurrence in the environment and in humans in China: not a negligible health risk due to the re-emergence of schistosomiasis, *Environ. Int.*, 2012, **42**, 105–116.

16 Y. Zhang, Y. Long, Z. Yuancheng, Y. Zhu, H. Wang, H. Wu and W. Lu, Effect of a mixed anionic–nonionic surfactant adsorption on bentonite structure and on distribution of pentachlorophenol, *Appl. Clay Sci.*, 2012, **69**, 93–98.

17 Y.-C. Cho, C.-C. Hsu and Y.-P. Lin, Integration of in-situ chemical oxidation and permeable reactive barrier for the removal of chlorophenols by copper oxide activated peroxydisulfate, *J. Hazard. Mater.*, 2022, **432**, 128726.

18 A. Shankar, M. Kongot, V. K. Saini and A. Kumar, Removal of pentachlorophenol pesticide from aqueous solutions using modified chitosan, *Arabian J. Chem.*, 2020, **13**, 1821–1830.

19 U. D. Patel and S. Suresh, Electrochemical treatment of pentachlorophenol in water and pulp bleaching effluent, *Sep. Purif. Technol.*, 2008, **61**, 115–122.

20 X. Cai, J. Li, F. Guan, X. Luo, Z. Yu and Y. Yuan, Complete pentachlorophenol biodegradation in a dual-working electrode bioelectrochemical system: Performance and functional microorganism identification, *Water Res.*, 2023, **230**, 119529.

21 S. Venkataraman and V. K. Vaidyanathan, Synthesis of magnetically recyclable porous cross-linked aggregates of Tramates versicolor MTCC 138 laccase for the efficient removal of pentachlorophenol from aqueous solution, *Environ. Res.*, 2023, **229**, 115899.

22 V. K. Vaidyanathan, P. S. Kumar, G. Rangasamy, R. G. Saratale and G. D. Saratale, Removal of pentachlorophenol and phenanthrene from lignocellulosic biorefinery wastewater by a biocatalytic/biosurfactant system comprising cross-linked laccase aggregates and rhamnolipid, *Environ. Pollut.*, 2023, **329**, 121635.

23 R. W. Ammeri, S. Kloula, G. D. R. Simeone, I. Mehri, W. Hassan and A. Hassen, Pesticide removal by the bioaugmentation process in secondary treated wastewater, *Water Qual. Res. J.*, 2023, **58**, 111–127.

24 Q. Chen, M. Zhou, Y. Pan and Y. Zhang, Ligand-Enhanced Zero-Valent Iron for Organic Contaminants Degradation: A Mini Review, *Processes*, 2023, **11**, 620.

25 S. Natarajan, H. C. Bajaj and R. J. Tayade, Recent advances based on the synergetic effect of adsorption for removal of dyes from waste water using photocatalytic process, *J. Environ. Sci.*, 2018, **65**, 201–222.

26 L. Huang, X. Huang, J. Yan, Y. Liu, H. Jiang, H. Zhang, J. Tang and Q. Liu, Research progresses on the application of perovskite in adsorption and photocatalytic removal of water pollutants, *J. Hazard. Mater.*, 2023, **442**, 130024.

27 L. Zhao, J. Deng, P. Sun, J. Liu, Y. Ji, N. Nakada, Z. Qiao, H. Tanaka and Y. Yang, Nanomaterials for treating emerging contaminants in water by adsorption and photocatalysis: Systematic review and bibliometric analysis, *Sci. Total Environ.*, 2018, **627**, 1253–1263.

28 M. H. Sayadi, S. Homaeigohar, A. Rezaei and H. Shekari, Bi/SnO_2/TiO_2.graphene nanocomposite photocatalyst for solar visible light–induced photodegradation of pentachlorophenol, *Environ. Sci. Pollut. Res.*, 2021, **28**, 15236–15247.

29 N. Boumahdi, A. Hadj-Ziane-Zafour, H. Yaiche-Achour and H. Khalaf, Preparation of Bi_2O_3/TiO_2–Montmorillonite Nanocomposites and Their Applications to the Photodegradation of

Pentachlorophenol, *Bull. Chem. React. Eng. Catal.*, 2022, **17**, 78–87.

30 F. S. Arghavan, A. Hossein Panahi, N. Nasseh and M. Ghadirian, Adsorption-photocatalytic processes for removal of pentachlorophenol contaminant using $FeNi_3$/SiO_2/ZnO magnetic nanocomposite under simulated solar light irradiation, *Environ. Sci. Pollut. Res.*, 2021, **28**, 7462–7475.

31 L. Yu, X. Yang, Y. Ye, X. Peng and D. Wang, Silver nanoparticles decorated anatase TiO_2 nanotubes for removal of pentachlorophenol from water, *J. Colloid Interface Sci.*, 2015, **453**, 100–106.

32 G. Nabi, W. Ali, M. Tanveer, T. Iqbal, M. Rizwan and S. Hussain, Robust synergistic effect of TiS_2/MoS_2 hierarchal micro-flowers composite realizing enhanced electrochemical performance, *J. Energy Storage*, 2023, **58**, 106316.

33 S. Bandow, F. Kokai, K. Takahashi, M. Yudasaka, L. Qin and S. Iijima, Interlayer spacing anomaly of single-wall carbon nanohorn aggregate, *Chem. Phys. Lett.*, 2000, **321**, 514–519.

34 T. Yamaguchi, S. Bandow and S. Iijima, Synthesis of carbon nanohorn particles by simple pulsed arc discharge ignited between pre-heated carbon rods, *Chem. Phys. Lett.*, 2004, **389**, 181–185.

35 M. Shapovalova, T. Khalyavka, O. Khyzhun, N. Shcherban, V. Permyakov and S. Scherbakov, The influence of titanium dioxide modification by sulfur and carbon on physicochemical and photocatalytic properties, *Him. Fiz. ta Tehnol. Poverhni.*, 2019, **10**, 377–388.

36 K. Mishra, S. H. Kim and Y. R. Lee, Band-Gap Narrowing of Highly Stable Heterogeneous ZrO_2–ZnO Nanocomposites for the Reductive Amination of Carbonyl Compounds with Formic Acid and Triethylamine, *ChemSusChem*, 2019, **12**, 881–889.

37 T. Soltani, A. Tayyebi and B.-K. Lee, $BiFeO_3$/$BiVO_4$ p–n heterojunction for efficient and stable photocatalytic and photoelectrochemical water splitting under visible-light irradiation, *Catal. Today*, 2020, **340**, 188–196.

38 P. Makuła, M. Pacia and W. Macyk, *How to correctly determine the band gap energy of modified semiconductor photocatalysts based on UV–Vis spectra*, ACS Publications, 2018, pp. 6814–6817.

39 Q. Wang, Y. Yao, X. Sang, L. Zou, S. Ge, X. Wang, D. Zhang, Q. Wang, H. Zhou and J. Fan, Photoluminescence and Electrical Properties of n-Ce-Doped ZnO Nanoleaf/p-Diamond Heterojunction, *Nanomaterials*, 2022, **12**, 3773.

40 D. Zhang, Z. Xue, Q. Wang and J. Ma, Violet and blue photoluminescence emitted from ZnO films deposited by rf magnetron sputtering, *Materials, Devices, and Systems for Display and Lighting*, SPIE, 2002, pp. 425–428.

41 L. Tsybeskov, J. V. Vandyshev and P. Fauchet, Blue emission in porous silicon: Oxygen-related photoluminescence, *Phys. Rev. B: Condens. Matter Mater. Phys.*, 1994, **49**, 7821.

42 P. V. Raleaooa, A. Roodt, G. G. Mhlongo, D. E. Motaung, R. E. Kroon and O. M. Ntwaeaborwa, Luminescent, magnetic and optical properties of ZnO–ZnS nanocomposites, *Phys. B*, 2017, **507**, 13–20.

43 S. P. Onkani, P. N. Diagboya, F. M. Mtunzi, M. J. Klink, B. I. Olu-Owolabi and V. Pakade, Comparative study of the photocatalytic degradation of 2–chlorophenol under UV irradiation using pristine and Ag-doped species of TiO_2, ZnO and ZnS photocatalysts, *J. Environ. Manage.*, 2020, **260**, 110145.

44 G. Hitkari, S. Singh and G. Pandey, Structural, optical and photocatalytic study of ZnO and ZnO–ZnS synthesized by chemical method, *Nano-Struct. Nano-Objects*, 2017, **12**, 1–9.

45 Y. Li, M. Jiao, H. Zhao and M. Yang, High performance gas sensors based on in-situ fabricated ZnO/polyaniline nanocomposite: the effect of morphology on the sensing properties, *Sens. Actuators, B*, 2018, **264**, 285–295.

46 C. Buttersack, Modeling of type IV and V sigmoidal adsorption isotherms, *Phys. Chem. Chem. Phys.*, 2019, **21**, 5614–5626.

47 L. W. Bingel and K. S. Walton, Surprising use of the business innovation bass diffusion model to accurately describe adsorption isotherm types I, III, and V, *Langmuir*, 2023, **39**, 4475–4482.

48 N. Satdeve, R. Ugwekar and B. Bhanvase, Ultrasound assisted preparation and characterization of Ag supported on ZnO nanoparticles for visible light degradation of methylene blue dye, *J. Mol. Liq.*, 2019, **291**, 111313.

49 G. G. Wallace, P. R. Teasdale, G. M. Spinks and L. A. Kane-Maguire, *Conductive electroactive polymers: intelligent polymer systems*, CRC press, 2008.

50 B. Muzikova, T. Marikova, J. Rathousky and M. Kuchar, The optimalization of photocatalytic degradation of 4-*tert*-octylphenol, *Ann. Toxicol. Anal.*, 2022, **34**, S148.

51 M. Evers, R.-L. Lange, E. Heinz and M. Wichern, Simultaneous powdered activated carbon dosage for micropollutant removal on a municipal wastewater treatment plant compared to the efficiency of a post treatment stage, *J. Water Proc. Engineering*, 2022, **47**, 102755.

52 F. Wang, F. Huang, F. Yu, X. Kang, Q. Wang and Y. Liu, Metal-sulfide photocatalysts for solar-fuel generation across the solar spectrum, *Cell Rep. Phys. Sci.*, 2023, **4**, 101450.

53 M. B. Tahir, M. Rafique, M. S. Rafique, N. Fatima and Z. Israr, Metal oxide-and metal sulfide-based nanomaterials as photocatalysts, *Nanotechnology and Photocatalysis for Environmental Applications*, Elsevier, 2020, pp. 77–96.

54 Z. Liu, J. Li, S. Liu, Y. Yuan, A. Chen, H. Yu, S. Wang, J. Ding and H. Fang, Suppressing Carrier Recombination in $BiVO_4$/PEDOT: PSS Heterojunction for High-Performance Photodetector, *J. Phys. Chem. Lett.*, 2024, **15**, 2476–2484.

55 A. Kagkoura and N. Tagmatarchis, Carbon nanohorn-based electrocatalysts for energy conversion, *Nanomaterials*, 2020, **10**, 1407.

56 Z. Y. Gao and H. Zhang, Photodegradation of pentachlorophenol using NiO-coupled $NiTiO_3$ nanocomposites from layered precursor as photocatalysts, *Adv. Mater. Res.*, 2012, **396**, 411–416.

57 J. Xie, Z. Zhou, Y. Lian, Y. Hao, P. Li and Y. Wei, Synthesis of α-Fe_2O_3/ZnO composites for photocatalytic degradation of

pentachlorophenol under UV-vis light irradiation, *Ceram. Int.*, 2015, **41**, 2622–2625.

58 F. Licht, M. Davis and H. Andreas, Charge redistribution and electrode history impact galvanostatic charging/discharging and associated figures of merit, *J. Power Sources*, 2020, **446**, 227354.

59 M. Azimzadeh Sani, N. G. Pavlopoulos, S. Pezzotti, A. Serva, P. Cignoni, J. Linnemann, M. Salanne, M. P. Gaigeot and K. Tschulik, Unexpectedly High Capacitance of the Metal Nanoparticle/Water Interface: Molecular-Level Insights into the Electrical Double Layer, *Angew. Chem.*, 2022, **134**, e202112679.

60 S. Dhillon and R. Kant, Theory for electrochemical impedance spectroscopy of heterogeneous electrode with distributed capacitance and charge transfer resistance, *J. Chem. Sci.*, 2017, **129**, 1277–1292.

61 Z. Jia, J. Liu, R. Li, C. Fan and Y. Wang, Bi_4O_7 modified $AgBiO_3$ to construct *Z*-scheme heterojunction for photocatalytic removing phenol, *Mater. Sci. Semicond. Process.*, 2024, **177**, 108359.

62 D. Zhou, D. Li and Z. Chen, Recent advances in ternary *Z*-scheme photocatalysis on graphitic carbon nitride based photocatalysts, *Front. Chem.*, 2024, **12**, 1359895.

63 T. M. Anh, T.-D. Pham, N. M. Viet, D. T. N. Anh, N. T. D. Cam, N. Van Noi, D. N. Nhiem, C. N. Chau, T. T. V. Ha and N. M. Phuong, Investigation of Diazinon degradation *via* advanced photocatalysis of $CoWO_4$/g-C_3N_4 *Z* scheme heterojunction with addition of H_2O_2, *Chem. Phys.*, 2024, **579**, 112166.

64 G. Ding, Z. Wang, J. Zhang, P. Wang, L. Chen and G. Liao, Layered double hydroxides-based *Z*-scheme heterojunction for photocatalysis, *EcoEnergy*, 2024, **2**, 22–44.

65 M. B. Tahir, M. S. Rafique, M. Sagir and M. F. Malikd, Role of Metal Oxide/Sulphide/Carbon-Based Nanomaterials in Photocatalysis, in *New Insights in Photocatalysis for Environmental Applications*, Briefs in Applied Sciences and Technology, Springer, 2022, pp. 39–47.

66 J. C. Conesa, Nanostructured sulfide based photocatalysts using visible light for environmental and energy purposes, in *Materials Science in Photocatalysis*, Elsevier, 2021, pp. 267–282.

67 A. Slesinski and E. Frackowiak, Metal Oxide Mixed Sulphide of Controlled Crystal Structure As Catalysts for Two-Electron Water Oxidation, in: Electrochemical Society Meeting Abstracts 244, The Electrochemical Society, Inc., 2023, pp. 2820-2820.

68 H. Zhang, Z. Wang, J. Zhang and K. Dai, Metal-sulfide-based heterojunction photocatalysts: Principles, impact, applications, and in-situ characterization, *Chin. J. Catal.*, 2023, **49**, 42–67.

69 G. Higginson, The effect of sulphur and oxygen on the electrical properties of oxide-coated cathodes, *Br. J. Appl. Phys.*, 1957, **8**, 148.

70 J. P. Fuentes, S. Jadoun, O. Yepsen, H. D. Mansilla and J. Yáñez, Prediction of band edge potentials and reaction products in photocatalytic copper and iron sulfides, *Photochem. Photobiol. Sci.*, 2023, **22**, 1855–1864.

71 H. Shi, G. Chen, C. Zhang and Z. Zou, Polymeric g-C_3N_4 coupled with $NaNbO_3$ nanowires toward enhanced photocatalytic reduction of CO_2 into renewable fuel, *ACS Catal.*, 2014, **4**, 3637–3643.

72 B. Lin, G. Yang, B. Yang and Y. Zhao, Construction of novel three dimensionally ordered macroporous carbon nitride for highly efficient photocatalytic activity, *Appl. Catal., B*, 2016, **198**, 276–285.

73 Z. Wang, L. Jiang, K. Wang, Y. Li and G. Zhang, Novel AgI/$BiSbO_4$ heterojunction for efficient photocatalytic degradation of organic pollutants under visible light: Interfacial electron transfer pathway, DFT calculation and degradation mechanism study, *J. Hazard. Mater.*, 2021, **410**, 124948.

74 Y. Xiao, X. Cui, B. Xiang, Y. Chen, C. Zhao, L. Wang, C. Yang, G. Zhang, C. Xie and Y. Han, $MDACl_2$-modified SnO_2 film for efficient planar perovskite solar cells, *Molecules*, 2023, **28**, 2668.

75 S. Li, M. Cai, Y. Liu, C. Wang, R. Yan and X. Chen, Constructing $Cd_{0.5}Zn_{0.5}S/Bi_2WO_6$ S-scheme heterojunction for boosted photocatalytic antibiotic oxidation and Cr(VI) reduction, *Adv. Powder Mater.*, 2023, **2**, 100073.

76 C. Cheng, Q. Fang, S. Fernandez-Alberti and R. Long, Depleted oxygen defect state enhancing tungsten trioxide photocatalysis: a quantum dynamics perspective, *J. Phys. Chem. Lett.*, 2022, **13**, 5571–5580.

77 X. Ke, J. Zhang, K. Dai, K. Fan and C. Liang, Integrated S-scheme heterojunction of amine-functionalized 1D CdSe nanorods anchoring on ultrathin 2D $SnNb_2O_6$ nanosheets for robust solar-driven CO_2 conversion, *Solar RRL*, 2021, **5**, 2000805.